

Effects of energy-dependent scatterings on fast neutrino flavor conversions

Chinami Kato

*Faculty of Science and Technology, Tokyo University of Science,
2641 Yamazaki, Noda-shi, Chiba Prefecture 278-8510, Japan**

Hiroki Nagakura

National Astronomical Observatory of Japan, 2-21-1 Osawa, Mitaka, Tokyo 181-8588, Japan

(Dated: July 21, 2022)

Neutrino self-interactions in a dense neutrino gas can induce collective neutrino flavor conversions. Fast neutrino flavor conversions (FFCs), one of the collective neutrino conversion modes, potentially change the dynamics and observables in core-collapse supernovae and binary neutron star mergers. In cases without neutrino-matter interactions (or collisions), FFCs are essentially energy-independent, and therefore the single energy treatment has been used in previous studies. However, neutrino-matter collisions in general depend on neutrino energy, suggesting that energy-dependent features may emerge in FFCs with collisions. In this paper, we perform dynamical simulations of FFCs with iso-energetic scatterings (emulating nucleon scatterings) under multi-energy treatment. We find that cancellation between in- and out-scatterings happens in high energy region, which effectively reduces the number of collisions and then affects the FFC dynamics. In fact, the lifetime of FFCs is extended compared to the single-energy case, leading to large flavor conversions. Our result suggests that the multi-energy treatment is mandatory to gauge the sensitivity of FFCs to collisions. We also provide a useful quantity to measure the importance of multi-energy effects of collisions on FFCs.

I. INTRODUCTION

In dense neutrino environments such as core-collapse supernovae (SNe), binary neutron star mergers (BNSMs), and early Universe, refractive effects by neutrino self-interactions can induce collective neutrino flavor conversions [1–4]. Under certain conditions, the growth rate of flavor conversion becomes proportional to the number density of neutrinos, which corresponds to a fast mode or fast flavor conversion (FFC). FFC is triggered when electron neutrino lepton number crossings (ELN crossings) appears in angular distributions of neutrinos [5]. Recent studies have indicated that ELN crossings are ubiquitous in SNe and BNSMs [6–24]. Since neutrino flavor conversions, in general, have a potential to affect the fluid dynamics, nucleosynthesis, and neutrino signals [8, 25–27], FFCs have garnered significant attention recently.

In SNe and BNSMs, neutrinos also undergo matter interactions (or collisions) during propagation through matter. The description of neutrino dynamics involving neutrino transport, flavor conversion, and neutrino-matter collisions requires quantum kinetic treatment. SNe- and BNSM simulations with quantum kinetic neutrino transport are, however, a formidable challenge for computational astrophysics. In fact, their global simulations with resolving small-scale variations of FFCs (see, e.g., [28–35]) are intractable at present. Currently feasible approach is either local simulations [28, 29, 31, 33, 34, 36–41] or global simulations with some simplifications and assumptions [26, 42–44].

Recently effects of collisions on FFCs have been also studied numerically [29, 45–49]. Some studies have found enhancement of FFCs by neutral-current-like matter collisions [45–47, 49], whereas others have reported damping effects [29, 48]. Although these results are apparently in conflict with each other, which may be due to different angular distributions of neutrinos [49] or self-consistency issues faced by homogeneous models [50], they are in agreement with a suggestion that collisions have non-negligible roles on FFCs. We also note that a new type of instability of flavor conversion, collisional flavor instability, may occur due to disparity of matter interactions between neutrinos and antineutrinos [51].

FFCs are purely driven by neutrino self-interactions, suggesting that energy dependent features induced by vacuum potential are smeared out¹. Hence, the energy-integrated QKEs or monochromatic assumption has been commonly used in the previous FFC studies. However, the approximation becomes inappropriate if neutrino-matter interactions are involved. Cross sections of weak current depend on energy, and the energy spectrum of neutrinos is not monochromatic in SNe/BNSMs, indicating that energy-dependent flavor conversions may be induced by collisions. In fact, recent studies showed that vigor of FFCs hinges on the reaction rate [49], and therefore it is of great interest to investigate FFCs with energy-dependent collisions in non-monochromatic neutrino energy spectrum.

In this paper, we perform dynamical simulations of FFCs in homogeneous background with incorporating

* ckato@rs.tus.ac.jp

¹ It should be noted that the vacuum potential plays a role as a seed perturbation to trigger FFCs.

energy-dependent collisions (iso-energetic scatterings). The goal of this paper is to understand the essence of multi-energy effects of iso-scatterings on FFCs. In so doing, a simple setup is adopted in our simulations. We find some qualitative differences of FFCs between single- and multi-energy treatments in the non-linear phase, which is scrutinized in this paper.

The paper is organized as follows. We start with describing basic equations and our numerical solver with a Monte Carlo method in Section II. Before entering into results of multi-energy FFC simulations, we revisit the case of those with energy-independent collisions in Section III A, which provides some clues to interpret multi-energy effects of collisions on FFCs. We then discuss FFCs with energy-dependent collisions in two cases: flat neutrino energy spectrum and non-flat spectrum in Sections III B and III C, respectively. Finally, we conclude and discuss our study in Section IV.

II. NUMERICAL SETUP

A. Basic equations

Time evolution of neutrinos in phase space follows the quantum kinetic equations (QKEs),

$$i \left(\frac{\partial}{\partial t} + \vec{v} \cdot \nabla \right) \rho(\vec{x}, \vec{p}, t) = [\mathcal{H}, \rho(\vec{x}, \vec{p}, t)] + i\mathcal{C}[\rho], \quad (1)$$

$$i \left(\frac{\partial}{\partial t} + \vec{v} \cdot \nabla \right) \bar{\rho}(\vec{x}, \vec{p}, t) = [\bar{\mathcal{H}}, \bar{\rho}(\vec{x}, \vec{p}, t)] + i\bar{\mathcal{C}}[\bar{\rho}]. \quad (2)$$

In this expression, ρ ($\bar{\rho}$) describes the density matrix for neutrinos (antineutrinos). The Hamiltonian potentials \mathcal{H} and $\bar{\mathcal{H}}$ include contributions from the neutrino mass difference, the coherent forward scattering with surrounding matters and other neutrinos as detailed in [2, 52]. \mathcal{C} and $\bar{\mathcal{C}}$ represent the collision terms.

We assume a two flavor system comprised of electron-type neutrinos (ν_e) and heavy-leptonic ones (ν_x). In this approximation, the density matrix has four independent components, i.e., ρ_{ee} , ρ_{xx} , $\text{Re}\rho_{ex}$ and $\text{Im}\rho_{ex}$. We set the mass difference of neutrinos to be 0, and the matter term is also neglected, just for simplicity. It is also assumed that neutrino distributions are spatial homogeneous and axial asymmetry in momentum space. For collision terms, we consider iso-energetic scatterings. The reaction rate depends on neutrino energy, but we assume that it is independent on propagation direction (i.e., isotropic scattering). The rates are also assumed to be the same among all the components of density matrices. Under these assumptions, QKEs can be rewritten

as

$$\begin{aligned} & i \frac{\partial \rho_a(E_\nu, \cos \theta_\nu, t)}{\partial t} \\ &= [\mathcal{H}_{\nu\nu}, \rho_a(E_\nu, \cos \theta_\nu, t)] \\ &+ i \int_{-1}^1 d \cos \theta'_\nu R(E_\nu) \rho_a(E_\nu, \cos \theta'_\nu, t) \\ &- i \int_{-1}^1 d \cos \theta'_\nu R(E_\nu) \rho_a(E_\nu, \cos \theta_\nu, t), \end{aligned} \quad (3)$$

$$\begin{aligned} & i \frac{\partial \bar{\rho}_a(E_\nu, \cos \theta_\nu, t)}{\partial t} \\ &= [\bar{\mathcal{H}}_{\nu\nu}, \bar{\rho}_a(E_\nu, \cos \theta_\nu, t)] \\ &+ i \int_{-1}^1 d \cos \theta'_\nu R(E_\nu) \bar{\rho}_a(E_\nu, \cos \theta'_\nu, t) \\ &- i \int_{-1}^1 d \cos \theta'_\nu R(E_\nu) \bar{\rho}_a(E_\nu, \cos \theta_\nu, t). \end{aligned} \quad (4)$$

In this expression, $\rho_a = \int \rho d\phi_\nu$ denotes the azimuthal-angle integrated density matrix. The Hamiltonians by neutrino self-interactions can be written as

$$\begin{aligned} \mathcal{H}_{\nu\nu} &= \sqrt{2}G_F \int \int \frac{E_\nu'^2 dE_\nu' d \cos \theta'_\nu}{(2\pi)^2} \\ &\times (1 - \cos \theta_\nu \cos \theta'_\nu) \\ &\times (\rho_a(E_\nu, \cos \theta'_\nu, t) - \bar{\rho}_a^*(E_\nu, \cos \theta_\nu, t)), \end{aligned} \quad (5)$$

$$\begin{aligned} \bar{\mathcal{H}}_{\nu\nu} &= \sqrt{2}G_F \int \int \frac{E_\nu'^2 dE_\nu' d \cos \theta'_\nu}{(2\pi)^2} \\ &\times (1 - \cos \theta_\nu \cos \theta'_\nu) \\ &\times (\rho_a^*(E_\nu, \cos \theta'_\nu, t) - \bar{\rho}_a(E_\nu, \cos \theta_\nu, t)). \end{aligned} \quad (6)$$

Regarding the reaction kernel $R(E_\nu)$, the energy dependence emulates nucleon scatterings, i.e., $R(E_\nu) = R_0(E_\nu/20\text{MeV})^2$. In this study, we adopt $\mu \equiv \sqrt{2}G_F n_\nu = 10 \text{ cm}^{-1}$, where n_ν denotes the number density of ν_e . This corresponds to $n_\nu \sim 1.56 \times 10^{33} \text{ cm}^{-3}$.

We refer [45] to set initial angular distributions of neutrinos. ν_e have isotropic angular distributions, whereas antineutrinos ($\bar{\nu}_e$) have anisotropic ones,

$$\begin{aligned} g_{ee,0}(\cos \theta_\nu) &= 0.5n_\nu, \\ \bar{g}_{ee,0}(\cos \theta_\nu) &= \left[0.47 + 0.05 \exp \left(-(\cos \theta_\nu - 1)^2 \right) \right] n_\nu, \end{aligned} \quad (7)$$

where g is defined as $g \equiv \int \rho_a E_\nu'^2 dE_\nu' / (2\pi)^3$. Those for ν_x and their antipartners ($\bar{\nu}_x$) are set to be 0 initially. At the beginning of simulations, we put a small perturbation on off-diagonal components of ρ_a by $\text{Im}g_{ex} = -\text{Re}g_{ex} = 10^{-6}g_{ee}$, to trigger FFCs. Note that the number density of anti-neutrinos \bar{n}_ν is $1.53 \times 10^{33} \text{ cm}^{-3}$, which is $\sim 2\%$ smaller than n_ν .

B. QKE-MC solver

We solve QKEs (Eqs. 3 and 4) using Monte-Carlo technique [46]. Our code is an extended version from our

classical MC neutrino transport solver [53]. This QKE-MC solver has a capability of handling neutrino transport, matter collisions and neutrino flavor conversions self-consistently. Below we describe the essence of our code.

In classical MC methods, each MC particle represents a bundle of neutrinos in a specific flavor state, and the assembly of these particles describes a neutrino distribution function in phase space. On the other hand, if flavor conversions happen, flavor states are no longer constant during propagation. Hence, we add a flavor degree of freedom to each MC particle. More specifically, we define a new matrix, particle-density-matrix (PDM), which is assigned to each MC particle; the assembly of the PDM represents the density matrix of neutrinos.

In our QKE-MC solver, we handle collisions and flavor conversions separately, which is essentially along with an operating-splitting method. Firstly, we determine what particles and their flavor states undergo scatterings². We create a new MC particle at each scattering point, and its flight direction is determined probabilistically with a scattering kernel. In the meantime, we compute the self-interaction potential of neutrinos, and then evolve the PDM on each MC particle with fourth-order Runge-Kutta method. It should be mentioned that feedback from collisions is not included here. After updating the PDM, we copy the scattering-experienced PDM from the original MC particle to newly created ones.

Statistical noise, which is inevitably generated by probabilistic computations of collisions in MC methods, is a major concern. This may compromise the accuracy of our simulations. To mitigate the problem without substantially increasing computational costs, we have developed a special technique. Firstly, we discretize the neutrino phase space similar to mesh-based methods. The flight direction of each MC particle is corrected at each timestep to match with the central value of the mesh-point where the particle resides. Although this prescription smears out a small scale structure in neutrino momentum space, it can be controlled by changing the mesh resolution. Secondly, the effective mean free path (EMFP) method is adopted. In essence, we reduce the rate of change in the PDM (a ($0 \leq a \leq 1$)) at each scattering event, meanwhile the scattering length is also reduced by a factor of a . This prescription increases the number of scattering of MC particles (hence, the statistics is improved) with sustaining the physical impact of collisions. It should be mentioned that the mean free time of collisions is much longer than the FFC timescale, implying that the number of scatterings during a single timestep is small. As a result, the numerical cost of computing collisions is subdominant compared to other operations; hence we can maintain the computational cost even if the number of scatterings is increased by the

EMFP prescription. We refer readers to [46] for more details of these techniques and a suite of code tests.

In this study, we deploy 128 bins in angular direction of neutrinos and adopt 50,000 MC samples in each angular bin. The control parameter of EMFP method is set to be $a = 10^{-3}$, which shows a good performance to reduce the statistical noise without increasing numerical cost. In multi-energy simulations, we use two energy meshes (see Sec. III B and III C). Although the energy resolution is low, it highlights the essential multi-energy effects of collisions on FFCs. The investigation resolving more realistic neutrino energy spectrum is postponed to future work.

III. RESULTS

In this study, we have 9 models in total with different numerical setups. In Section III A, we first show results of FFC simulations with energy-independent collisions, in which we adopt a single-energy mesh. We then present results of multi-energy FFC simulations with energy-dependent collisions in Sections III B and III C. In the former section, we study cases with flat neutrino-energy spectrum, which illustrate the essence of multi-energy effects of collisions. In the latter one, we delve into the impact of non-flat neutrino-energy spectrum.

A. Energy-independent collisions

Here we revisit effects of energy-independent collisions on FFCs. We consider three cases with different reaction rates: $R_0 = 0$ (noscat), 1.25×10^{-5} (LR), $1.25 \times 10^{-4} \text{ cm}^{-1}$ (HR), assuming $R(E_\nu) = R_0(E_\nu/20\text{MeV})^2$ with $E_\nu = 20 \text{ MeV}$. These models are referred to E1 models hereafter.

Figure 1(a) portrays time evolution of ν_x 's number density, or $n_x \equiv \int d\cos\theta_\nu g_{xx}$ for E1 models. Since g_{xx} is initially zero (see Section II), the appearance of ν_x exhibits occurrence of flavor conversions. We also note that the trace of density matrix is not affected by flavor conversions, and iso-energetic scattering does not change the total number of neutrinos, implying that $n_e + n_x$ is a conserved quantity in our models. Black line describes the results without collisions (noscat), in which the time evolution of n_x has a periodic feature with a constant amplitude. This is consistent with previous studies [45], and this feature may be understood through a pendulum model [54, 55]. In cases with collisions, on the other hand, the periodic feature disappears. Although the amplitude of oscillations is smaller than that in the case without collisions, n_x increases with time, and eventually being saturated at a certain point (see cyan and green lines in Figure 1(a)). In these models, the saturation densities of ν_x become higher than the peak of ν_x in the case without collisions, indicating that collisions enhance flavor conversions.

² We assign a scattering distance to each element of the PDM.

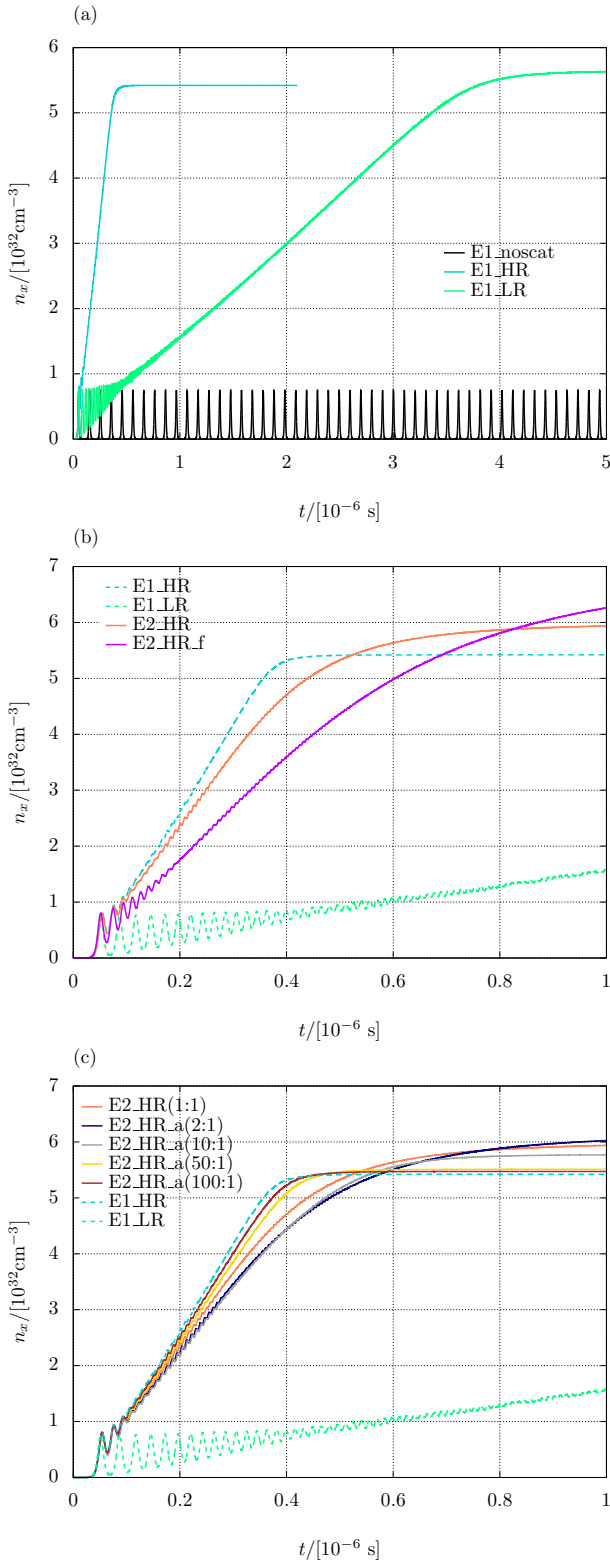


FIG. 1. Time evolution of n_x for (a) E1, (b) E2_HR and (c) E2_HR_a models. Black line in panel(a) describes the result without collisions. Other colors distinguish the models with collisions. In panels(b) and (c), the solid and dashed-lines represent E2 and E1 models, respectively.

The top panels in Figure 2 show angular distributions of ELN-XLN, or $L(\cos\theta_\nu) \equiv g_{ee}(\cos\theta_\nu) - g_{xx}(\cos\theta_\nu) - \bar{g}_{ee}(\cos\theta_\nu) + \bar{g}_{xx}(\cos\theta_\nu)$ at some selected times. As discussed in [42], ELN-XLN angular distributions characterize the growth of FFCs³. In the case without collisions (left-top panel), the angular distribution of L does not evolve much with time except in the vicinity of ELN-XLN crossing. As a result, the ELN-XLN crossing does not disappear throughout the evolution. In cases with collisions, on the other hand, the angular point where the ELN-XLN crossing occurs changes with time, and eventually the crossing disappears (L becomes positive in all directions). Around the time when the ELN-XLN crossing disappears ($t \sim 4 \times 10^{-7}$, 4×10^{-6} s for E1_HR and E1_LR models, respectively), n_x is saturated, indicating that FFCs subside. Since angular distributions of neutrinos are still anisotropic at the saturation time, they continue to be isotropized by collisions. The isotropization does not generate new ELN-XLN crossings, and therefore FFCs are no longer revived.

One of the important roles of collisions on FFC is to broaden the angular region where FFC occurs. As shown in left bottom panel of Figure 2, g_{ee} (\bar{g}_{ee}) in E1_noscat model decreases due to FFCs only around the region where L is zero ($\cos\theta_\nu \sim 0.2$). For cases with collisions, on the other hand, FFCs occur in the wider angular range (see middle- and right bottom panels of Figure 2). This is consistent with our observation that the ELN-XLN crossing point moves to forward angular directions due to isotropization by collisions.

To measure the anisotropy of ν_e , we define δ as

$$\delta = \left| \frac{\int d\cos\theta_\nu \cos\theta_\nu g_{ee}(\cos\theta_\nu)}{\int d\cos\theta_\nu g_{ee}(\cos\theta_\nu)} \right|, \quad (8)$$

and its time evolution is displayed in Figure 3(a). In the case without collisions (black line), δ has a periodic feature, which is the same trend as n_x . Green and cyan lines depict the results for E1_LR and E1_HR models, respectively. In these models, δ increases due to FFCs until the disappearance of the ELN-XLN crossing. After FFCs are terminated, δ monotonically decreases by collisions.

As shown in Figure 1(a), we find that the vigor of FFCs is stronger with increasing reaction rate, meanwhile the saturation amplitude and its time become smaller and shorter, respectively; those for E1_HR model (E1_LR model) are $n_x \sim 5.5 \times 10^{32} \text{ cm}^{-3}$ and $t \sim 4 \times 10^{-7}$ s ($n_x \sim 5.6 \times 10^{32} \text{ cm}^{-3}$ and $t \sim 4 \times 10^{-6}$ s). This exhibits that the

³ There is a caveat, however. In homogeneous models, the appearance of ELN or ELN-XLN crossings does not guarantee the occurrence of FFC. This is due to the fact that the instability would occur in inhomogeneous modes, while flavor conversion may be stable in homogeneous ones. Nevertheless, ELN-XLN angular distributions are still informative to understand qualitative trends of FFCs in homogeneous models. In fact, the disappearance of ELN-XLN angular crossings guarantees that FFC does not occur in homogeneous models.

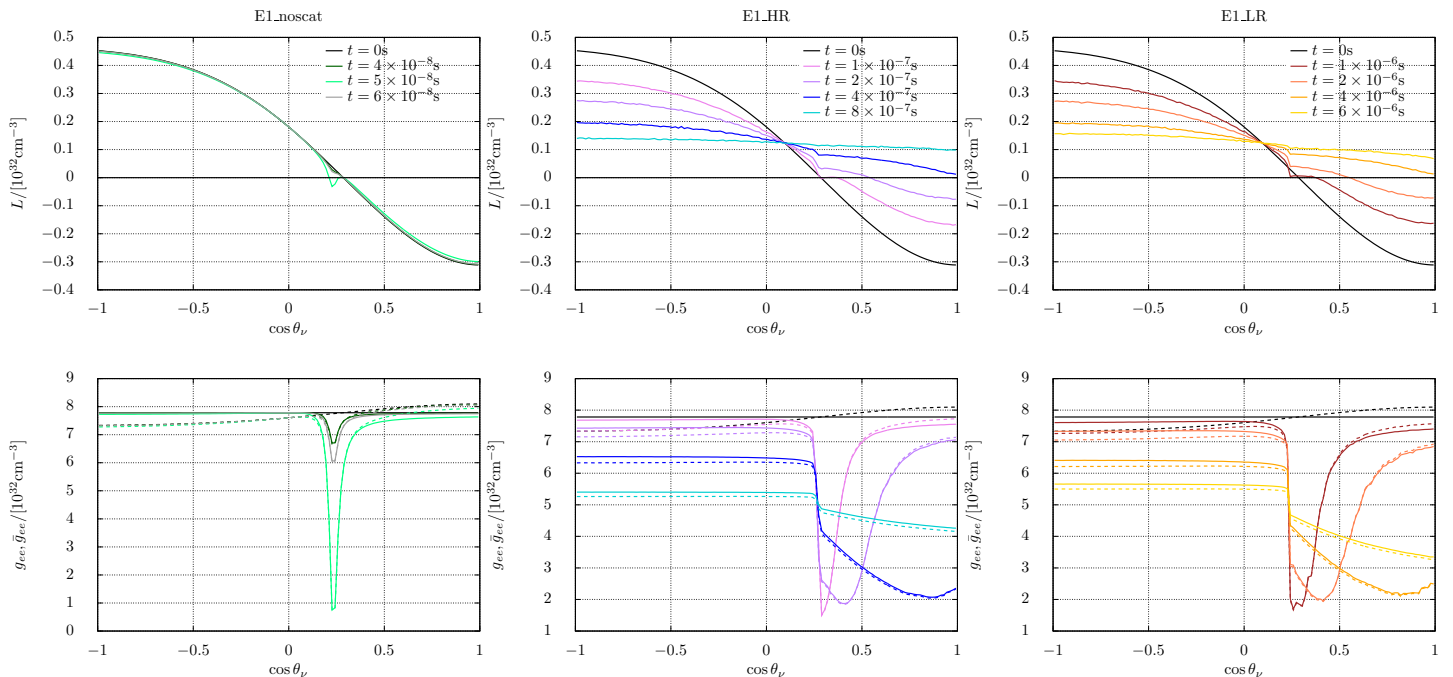


FIG. 2. Angular distributions of L (top) and g_{ee} (bottom) for E1 models. From the left panels, we show the results of E1_noscat, E1_HR and E1_LR models, respectively. Different colors denote different timesteps.

saturation amplitude of FFCs is determined through the competition between the growth rate and the duration of FFCs. This trend needs to be kept in our mind in the following discussions. It should also be mentioned that our results presented in this section is consistent with previous studies [45, 47, 49]. In the following subsections, we turn our attention to multi-energy effects of collisions on FFCs, which is the subject of this paper.

B. Energy-dependent collisions: flat neutrino-energy spectrum

Here, we discuss multi-energy effects of collisions on FFCs with comparing to the case of energy-independent collisions presented in Section III A. For the sake of simplicity, neutrino energies are assumed to be $E_{\text{low}} = 10$ MeV or $E_{\text{high}} = 30$ MeV. We refer to the models as E2. In this section, we consider the case with flat neutrino-energy spectrum, i.e., $n_{\text{low}} = n_{\text{high}} = n_{\nu}/2$ where n_{low} and n_{high} denote the numbers of neutrinos with the energy of E_{low} and E_{high} , respectively. We note that the case of non-flat energy spectrum will be discussed in the next subsection.

The angular distributions of neutrinos are set to be identical to those used in previous subsection (see Eqs. 7). This guarantees that the neutrino self-interaction potential at the beginning of simulation is identical among all models. We assume that the reaction rate is proportional to E_{ν}^2 emulating the energy dependence of neutral current

scatterings (see Eqs. 3 and 4). To discuss multi-energy effects of collisions appropriately, we set the reaction rate so that the energy-integrated rate becomes the same as that of E1_HR model. More specifically, we determine R_0 with a condition that the energy-averaged reaction rate for ν_e ,

$$\langle R_{ee} \rangle = \frac{R(E_{\text{low}})n_{\text{low}} + R(E_{\text{high}})n_{\text{high}}}{n_{\nu}}, \quad (9)$$

becomes $R_{\text{HR}} = 1.25 \times 10^{-4} \text{ cm}^{-1}$, which corresponds to the reaction rate used in E1_HR model. The resultant reaction rates at the energy of E_{low} and E_{high} are $R(E_{\text{low}}) = 2.50 \times 10^{-5} \text{ cm}^{-1}$ and $R(E_{\text{high}}) = 2.25 \times 10^{-4} \text{ cm}^{-1}$, respectively, and the correspond R_0 is 10^{-4} cm^{-1} . We name this model as a E2_HR model.

The time evolution of n_x in E2_HR model is depicted with a coral line in Figure 1(b). In the early phase, the time evolution of n_x in E2_HR model is almost identical to that of E1_HR model. After the time of $t \sim 10^{-7}$ s, differences between the two models become perceptible. The growth rate of n_x in E2_HR model becomes smaller than E1_HR model, whereas the saturation amplitude of n_x becomes higher. We have already witnessed the same trend when we compared the time evolution of n_x between E1_HR and E1_LR models (see Section III A). Following the same argument, our result suggests that the frequency of collisions in E2_HR model is reduced by multi-energy effects.

By comparing between the bottom-middle panel of Figure 2 and the left-top panel of Figure 4 (displaying g_{ee}

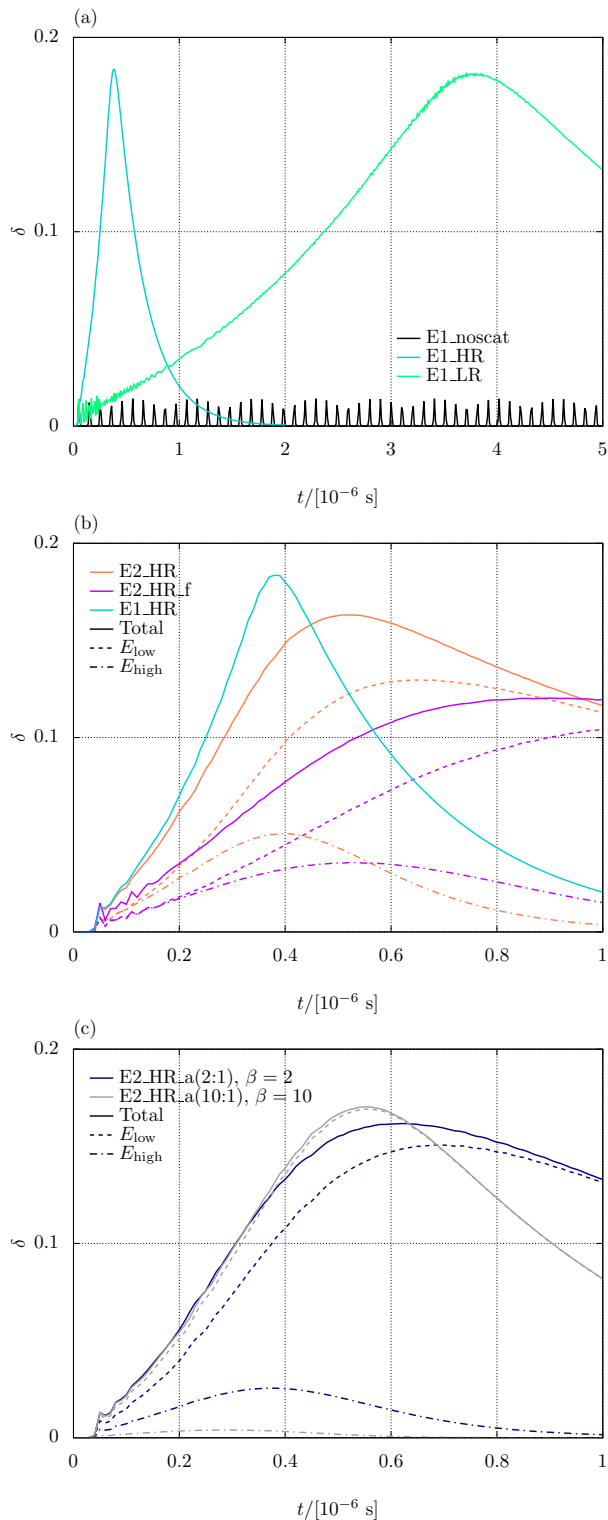


FIG. 3. Time evolution of δ for (a) E1, (b) E2_HR and (c) two selected E2_HR_a models. Colors distinguish the models. Solid lines describe δ with energy-integrated angular distributions in eq.8 (Total), while the dashed and dash-dotted lines denote those of low- (E_{low}) and high-energy neutrinos (E_{high}), respectively. For the low- (high-) energy case, we replace g_{ee} to $g_{ee,low}$ ($g_{ee,high}$) in the numerator of Eq.8.

and \bar{g}_{ee} as a function of neutrinos directional cosines in momentum space), the trend of weak collisions of E2_HR model can also be seen. The isotropization of ν_e is slower in E2_HR model than E1_HR model; consequently the δ in E2_HR model also increases more slowly than that in the E1_HR model, which is shown in Figure 3(b). We also find that FFCs in E2_HR model occur at the narrower angular range than in E1_HR model, which is consistent with the trend found in the case of low reaction rate of energy-independent collisions.

One of the keys to understand the difference between E1_HR and E2_HR models is rolls of collisions on high-energy neutrinos. In the middle and right panels of Figure 4, we display angular distributions of neutrinos at the energy of E_{low} and E_{high} , respectively. We note that $g_{ee,low}$ and $g_{ee,high}$ are the energy-integrated angular distributions for low- and high-energy neutrinos; hence, they satisfy the condition of $g_{ee} = g_{ee,low} + g_{ee,high}$. Since high-energy neutrinos experience collisions more frequently than those in E1_HR model ($R(E_{high}) > R_{HR}$), the angular distribution becomes more isotropic. As a result, the cancellation between in- and out-scatterings happens, which accounts for the effective reduction of collisions in E2_HR model. This feature can also be seen in the time evolution of δ . We display them for E_{low} and E_{high} as dashed and dash-dotted coral lines, respectively, in Figure 3(b).

To check if our interpretation that the scattering-balances happening in high-energy neutrinos is responsible for the difference of FFCs between energy-dependent and independent collisions is correct, we perform another simulation (E2_HR_f model), in which the angular distribution of high-energy $\bar{\nu}_e$'s is set to be isotropic at the beginning of the simulation. We also change the initial angular distribution of low-energy $\bar{\nu}_e$'s so as to be the same energy-integrated angular distributions of E2_HR model, which guarantees that the neutrino self-interaction becomes identical to that of E2_HR model. If the cancellation between in- and out-scatterings is a key of multi-energy effects, FFC dynamics in E2_HR_f model further deviates from E1_HR than the case of E2_HR.

As shown in Figure 1(b), the growth rate of n_x for E2_HR_f model (purple) is slower but the saturation amplitude becomes higher than those in E2_HR model (coral), that supports our interpretation. The time evolution of δ displayed in Figure 3(b) also provide another metric for this check. As shown in the purple lines, δ is less energy-dependent up to the time of $\sim 2 \times 10^{-7}$ s for E2_HR_f model (purple), meanwhile the energy-dependence appears in the earlier phase for E2_HR model (coral). This exhibits that effects of collisions in E2_HR_f model are more suppressed than E2_HR model. In the late phase, on the other hand, the energy-integrated δ gradually increases with time, and eventually it becomes higher than that of E2_HR model. We also display the angular distribution of ν_e and $\bar{\nu}_e$ for E2_HR_f model in bottom panels of Figure 4, and we find that the time evolution is slower than E2_HR model (displayed in the

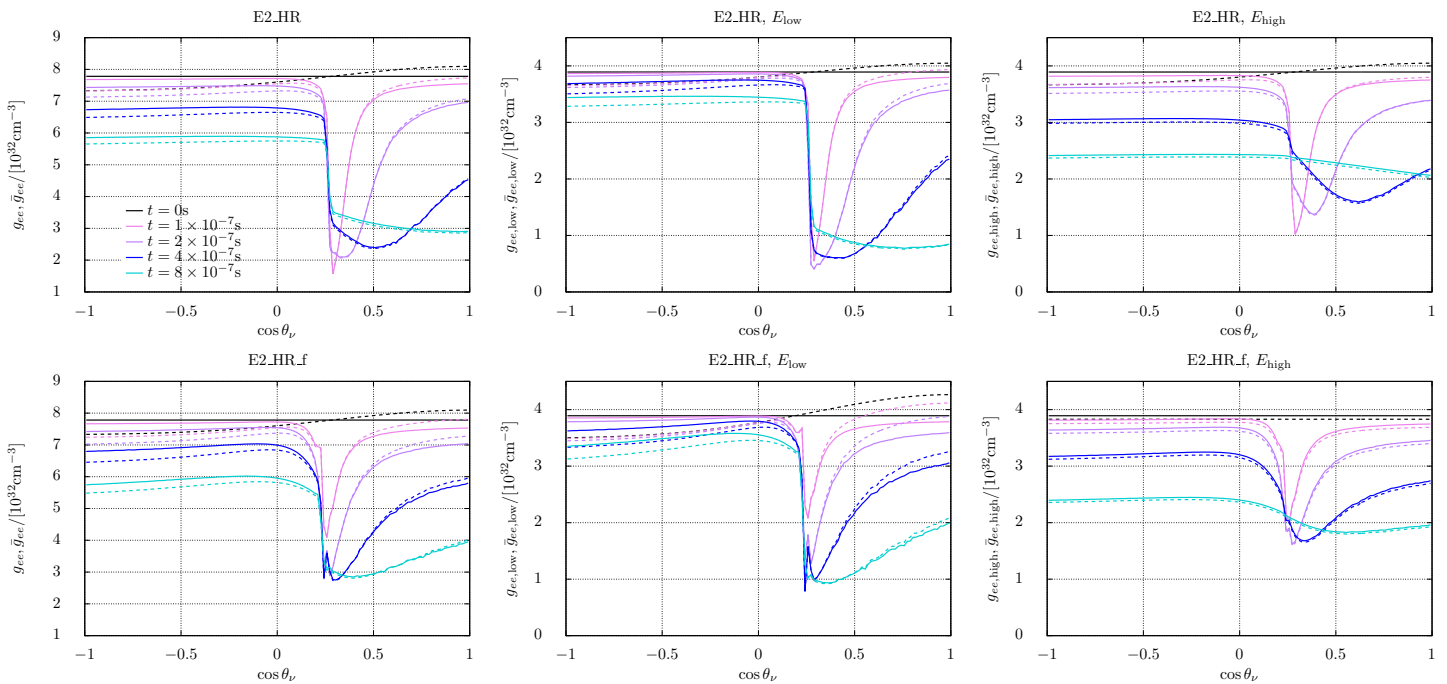


FIG. 4. Angular distributions for E2_HR (top), E2_HR.f models (bottom). The energy-integrated distributions are shown in the left panels, and those for low- and high neutrino energy are plotted in the middle and right panels, respectively. Different colors denote the different timesteps, which are the same as those selected in Figure 2 (for E1_HR model). Solid and dashed lines describe ν_e and $\bar{\nu}_e$, respectively.

top panels of the same figure). All these results are consistent with our claim that the cancellation between in- and out-scatterings plays a primary role in the deviation of FFCs from those with energy-independent collisions.

To quantify the energy-dependent flavor conversions, we define a transition probability from ν_e to ν_x as,

$$\langle P_{ex,i} \rangle = 1 - \frac{\int g_{ee,i} d \cos \theta_\nu}{\int g_{ee,i0} d \cos \theta_\nu}, \quad (10)$$

with $i = \text{low or high}$. We display them for E2_HR and E2_HR.f models in the top panel of Figure 5. Solid and dash-dotted lines represent the cases of low- and high-energy neutrinos, respectively. As shown in the figure, the transition probability is always higher in the case of high-energy neutrinos, which is due to effects of collisions; in fact the growth rate of FFCs becomes higher with increasing reaction rate (see Section III A). It is worthy to note that flavor conversions in high energy region do not stop even if their angular distributions become nearly isotropic. In fact, the saturation time of $\langle P_{ex,i} \rangle$ does not depend on energy. This exhibits that flavor conversions are driven by energy-integrated neutrino distributions, which is consistent with a property of FFCs.

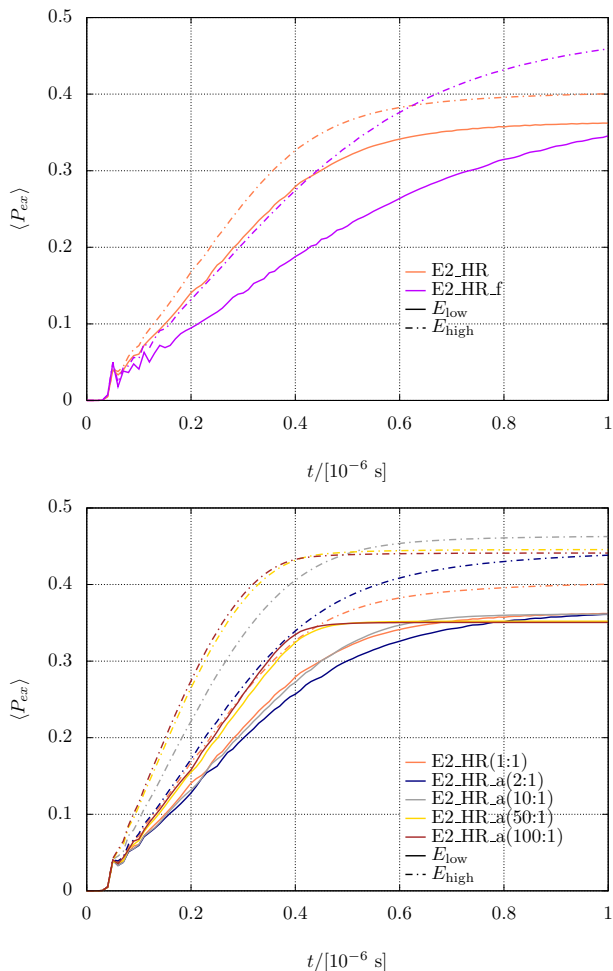
C. Energy-dependent collisions: non-flat neutrino-energy spectrum

It is an intriguing question how the above result (flat neutrino-energy spectrum) is altered in non-flat energy spectrum, i.e., $n_{\text{low}} \neq n_{\text{high}}$. Addressing the question is also important in studying for FFCs in SNe or BNSMs; in fact energy spectrum of neutrinos are non-monochromatic in these environments. In this subsection, we study the case with non-flat neutrino energy spectrum, in which we use E2_HR model as a reference to determine the numerical setups. The models which we study in this section are referred to as E2_HR_a models hereafter.

We consider 5 models with $n_{\text{low}}:n_{\text{high}} = 1:1, 2:1, 10:1, 50:1$ and $100:1$, satisfying a condition of $n_{\text{low}} + n_{\text{high}} = n_\nu$, initially. We note that the model with $n_{\text{low}} = n_{\text{high}}$ corresponds to E2_HR model. In the following discussions, we use the degree of neutrino-number-asymmetry ($\beta \equiv n_{\text{low}}/n_{\text{high}}$) to specify models. As with the case of flat energy spectrum, neutrino energies are set to be $E_{\text{low}} = 10$ MeV and $E_{\text{high}} = 30$ MeV; we control the coefficient R_0 so that the average reaction rates become $R_{\text{HR}} = 1.25 \times 10^{-4} \text{ cm}^{-1}$ (see Eq. 9). We note that R_0 increases with β , since the dominance of low-energy neutrinos requires higher R_0 so as for $\langle R_{ee} \rangle$ to be R_{HR} . The initial angular distributions of g 's are adopted from Eqs. 7, and the shapes are energy-independent. The setup pa-

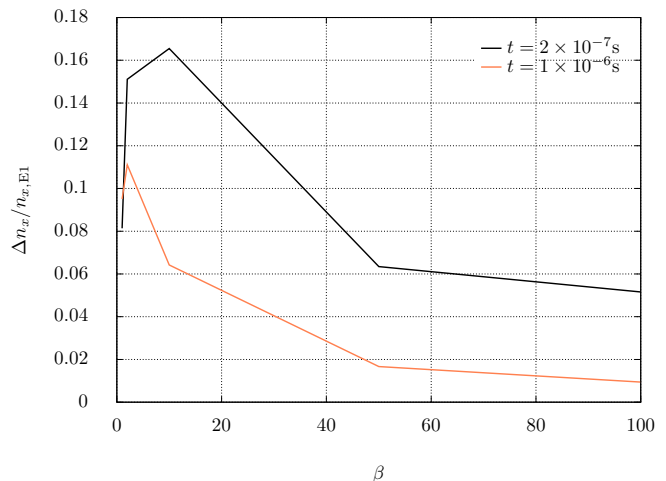
	$R_0/[10^{-4}\text{cm}^{-1}]$	n_{low}/n_ν	n_{high}/n_ν	β	$R_{\text{low}}/[10^{-4}\text{cm}^{-1}]$	$R_{\text{high}}/[10^{-4}\text{cm}^{-1}]$	$R_{\text{low}}n_{\text{low}}/R_{\text{high}}n_{\text{high}}$	χ
E2_HR(1:1)	1.00	1/2	1/2	1	0.25	2.25	0.111	0.167
E2_HR_a(2:1)	1.36	2/3	1/3	2	0.34	3.06	0.222	0.225
E2_HR_a(10:1)	2.89	10/11	1/11	10	0.72	6.50	1.11	0.245
E2_HR_a(50:1)	4.32	50/51	1/51	50	1.08	9.72	5.56	0.113
E2_HR_a(100:1)	4.63	100/101	1/101	100	1.16	10.4	11.0	0.078

TABLE I. Setups of E2_HR and E2_HR_a models.

FIG. 5. Time evolution of $\langle P_{ex} \rangle$ for E2_HR (top) and E2_HR_a models (bottom). Colors distinguish the models. Solid and dash-dotted lines denote the cases of low- and high-energy neutrinos, respectively.

parameters are summarized in Table I.

We find that all models have essentially the same trend as that found in the flat spectrum; the time evolution of FFCs tends to deviate towards the case with lower reaction rate in energy-independent collisions. More specifically, the n_x saturation values and times in the asymmetric models are larger and later than those in E1_HR model, respectively, which can be seen in Figure 1(c) (see solid lines and cyan-dotted, where the former denotes

FIG. 6. β dependence of Δn_x (normalized by $n_{x,E1}$). Results at two time snapshots are displayed: $t = 2 \times 10^{-7}$ s (black) and 1×10^{-6} s (coral).

E2_HR_a models and the latter is for E1_HR model). This strengthens our conclusion that the essence of multi-energy effects of collisions on FFCs is to reduce the reaction rate effectively due to cancellations between in- and out-scatterings at high-energy neutrinos.

Although the overall trend is the same as the case of flat energy spectrum, the detailed feature of FFCs depends on the spectrum. To measure the sensitivity quantitatively, we use the absolute difference of n_x from that of E1_HR model, i.e., $\Delta n_x \equiv |n_x - n_{x,E1}|$, where $n_{x,E1}$ denotes the n_x for E1_HR model. In Figure 6, we display them (normalized by $n_{x,E1}$) as a function of β .

Firstly, we focus on the early phase. Black line in this figure portrays Δn_x at $t = 2 \times 10^{-7}$ s. As shown in the figure, Δn_x is a non-monotonic dependence on β . This is attributed to the fact that E2_HR_a models are identical with E1_HR model in the limits of $\beta \rightarrow 0$ and ∞ . We find that Δn_x has a single peak, which is located at $\beta = 10$. To understand this trend, we consider a ratio of $R \times n$ between low- and high-energy neutrinos, which can be written as a function of β ,

$$\frac{R_{\text{low}}n_{\text{low}}}{R_{\text{high}}n_{\text{high}}} = \frac{1}{9}\beta \left(\frac{E_{\text{low}}}{10\text{MeV}} \right)^2 \left(\frac{E_{\text{high}}}{30\text{MeV}} \right)^{-2}. \quad (11)$$

In the region of $0 \leq \beta < 9$, effects of collisions are dominated by high-energy neutrinos. In this region, Δn_x

monotonically increases with β , since the dominance of high-energy neutrinos decreases with β . On the contrary, in the region of $\beta > 9$, low-energy neutrinos dominate over high-energy ones in effects of collisions on FFCs, and the dominance of collisions in low-energy neutrinos becomes stronger with increasing β . As a result, the system approaches the single-energy case (Δn_x becomes smaller) with increasing β . The result of our simulations agrees with this argument; in fact Δn_x would be the largest deviation around the point where the ratio of $R \times n$ becomes unity, i.e., $\beta \sim 9$ (see Eq. 11).

In the late phase, on the other hand, the situation becomes more complicated. As shown in a coral line in Figure 6, the model with the maximum Δn_x is not the same as that in the early phase; the model with $\beta = 2$ gives the maximum of Δn_x . The shift of β for the maximum Δn_x can be understood through the time evolution of δ , which is displayed in Figure 3(c). In the figure, we display results of $\beta = 2$ and 10 models in navy and gray lines, respectively. As shown by the solid lines, δ for the energy-integrated angular distributions in the $\beta = 10$ model is higher than that in the $\beta = 2$ one until $t \sim 6 \times 10^{-7}$ s. This is consistent with $R \times n$ diagnostics. In the later phase, however, δ in the $\beta = 2$ model becomes higher than the $\beta = 10$ one, which accounts for the shift of peak β for Δn_x . The slow but long-time increase of δ in the $\beta = 2$ model is attributed to the fact that R_{low} in the $\beta = 2$ model is lower than that in the $\beta = 10$ one; consequently, the life time of FFCs in the $\beta = 2$ model becomes longer (see Section III A). This exhibits the reason why $R \times n$ diagnostics can not estimate β which gives the maximum Δn_x in the late phase. As can be seen in the left hand side of Eq. 11, the R_0 dependence in R_{low} and R_{high} is canceled with each other in the diagnostics; consequently, the lifetime of FFCs is not taken into account in the diagnostics.

It should be emphasized, however, that the deviation of the peak β is not significant, and the qualitative dependence of Δn_x on β can be captured appropriately by the ratio of $R \times n$. Hence, the diagnostics is still informative to exhibit the dependence of Δn_x on β qualitatively.

There is one more caveat in the diagnostics, however. The ratio can be only taken for $N_\varepsilon = 2$, where N_ε denotes the number of energy mesh, indicating that it is not applicable in cases with $N_\varepsilon \geq 3$. In general, it is necessary for $N_\varepsilon \geq 3$ to capture complex shapes of neutrino energy spectrum in SNe and BNSM environments. We thus consider another diagnostic quantity, which can be applied to an arbitrary energy spectrum of neutrinos.

To this end, we define average energy of neutrinos,

$$\langle E_\nu \rangle = \frac{\int d^3\vec{p} E_\nu \rho}{\int d^3\vec{p} \rho}, \quad (12)$$

and its R -weighted energy,

$$\langle RE_\nu \rangle = \frac{\int d^3\vec{p} R E_\nu \rho}{\int d^3\vec{p} R \rho}. \quad (13)$$

Both energies become identical if all neutrinos have the same energy or R is energy-independent. This suggests that the difference of the two average energies represents effects of multi-energy of collisions. Motivated by the above consideration, we propose a variable χ as a diagnostic quantity of multi-energy effects of collisions on FFCs, which is defined as

$$\chi = \left| \frac{\langle E_\nu \rangle - \langle RE_\nu \rangle}{\langle E_\nu \rangle + \langle RE_\nu \rangle} \right|. \quad (14)$$

The values for all models are listed in Table I. As shown in the table (see the second and first columns from the right), χ and the $R \times n$ diagnostics have the same dependence on β ; in fact χ has a non-monotonically dependence on β , and it becomes maximum at $\beta = 10$ in our models. It should be emphasized that χ can be computed with respect to an arbitrary energy spectrum; hence, it would be useful to diagnose multi-energy effects of collisions on FFCs for cases with more complex energy-spectrum.

Finally, we show the time evolution of $\langle P_{ex} \rangle$ in the bottom panel of Figure 5. The figure illustrates the impact of energy dependence of collisions on FFCs in models with non-flat energy spectrum. This leads us to a robust conclusion that multi-energy effects of collisions induce energy-dependent features in FFCs, and the mixing degree sensitively depends on neutrino energy spectrum.

IV. SUMMARY AND DISCUSSIONS

Recent studies have indicated that fast neutrino flavor conversion (FFC), one of neutrino oscillations induced by neutrino self-interaction, occurs in SNe or BNSMs. However, there is still little known about the non-linear dynamics. One of unresolved issues is the interplay between FFCs and neutrino-matter collisions, which is the main focus of this paper.

FFCs are essentially energy-independent; hence, almost all previous studies have taken the monochromatic or energy-integrated assumption. On the other hand, neutrino-matter collisions are in general energy-dependent, suggesting that the energy-integrated assumption may discard some potentially important effects of collisions on FFCs.

Motivated by this fact, we perform dynamical simulations of FFCs with iso-energetic scatterings by our QKE-MC solver [46]. We start with revisiting the case of energy-independent collisions in Section III A. The n_x evolution without collisions has a periodic feature with a constant amplitude, while n_x increases with small oscillations, and eventually it reaches the saturation at a certain time in the case with collisions. There are also clear differences in angular distributions of neutrinos between with and without collisions. In the case without collisions, FFCs occur in a very narrow angular region, which is due to the fact that the ELN-XLN angular crossing point is almost constant with time. In cases with collisions, on the other hand, the crossing point becomes

dynamical due to effects of collisions; consequently, FFCs occur in wider angular regions than the case without collisions. We also find that FFCs in higher-reaction rate model grow faster, but they are saturated at earlier time. As a result, the saturation value of n_x tends to be smaller with increasing the reaction rate.

In Section III B, we investigate effects of energy-dependent collisions on FFCs under the assumption of flat neutrino-energy spectrum. To capture the qualitative trend, we study the impact with two energy meshes. The energy dependence of reaction rate is proportional to E_ν^2 , emulating neutrino-nucleon scatterings ($R \propto E_\nu^2$). Our simulations show the clear difference between energy-independent and dependent collisions; the latter tends to be similar evolution as that with a lower reaction rate in the energy-independent collision. This is because high-energy neutrinos experience collisions more frequently, implying that their angular distributions become more isotropic. As a result, in- and out-scatterings are cancelled out each other, which accounts for reducing the number of collisions effectively. We also find that the transition probability $\langle P_{ex} \rangle$ depends on neutrino energy, exhibiting the importance of multi-energy treatment in studying FFCs with collisions.

In Section III C, we discuss the case of non-flat neutrino-energy spectrum. The overall trend is in line with the case of flat energy-spectrum; in fact, FFCs slowly evolve with time, but its lifetime becomes longer due to the effective reduction in the number of collisions. On the other hand, the detailed feature of FFCs depends on the energy-spectrum, and we find that the large deviation from the case with energy-independent collisions happens when β ($\equiv n_{\text{low}}/n_{\text{high}}$) is between 1 and 10. This result can be interpreted through the $R \times n$ ratio (see Eq. 11), although the diagnostic is limited only in the two energy meshes. We, hence, generalize the diagnostics by χ (see Eq. 14), which can be applied to an arbitrary neutrino-energy spectrum. This would be useful in studying impacts of collisions on FFCs in more general situations such as SNe and BNSMs environments. It should also be mentioned that the transition probability of flavor conversion is energy-dependent, which also sensitively depends on the neutrino-energy spectrum. Our finding opens a new path to create energy-dependent flavor conversions driven by FFCs, which should be distinct

from the slow mode.

Obviously, we imposed many assumptions and simplifications in the present study. Although these conditions are useful to highlight effects of energy-dependent collisions on FFCs, they should be relaxed for more realistic situations. The top priority would be to get rid of homogeneous condition. As is well known, the homogeneous condition restricts the dynamics of FFCs [28, 29, 31, 33], and more importantly, it also faces a self-consistency issue to consider effects of collisions on flavor conversions [50]. It is also an intriguing question how other collision terms, (emissions, absorptions, inelastic scatterings, and pair processes) create energy-dependent features in FFCs. We leave the investigation on these remaining issues to future work.

It should be stressed, however, that our main conclusion, emergence of energy-dependent FFCs induced by collisions, would not be changed in more realistic situations. Hence, it is particularly interesting to delve into FFCs in high-energy neutrinos with energy-dependent collisions; the reason is as follows. In classical neutrino transport, those neutrinos tend to be in thermal/chemical equilibrium with matter due to strong neutrino-matter coupling. Since the equilibrium state hinges on a neutrino flavor, the competition between FFCs and neutrino-matter interactions would happen. This competition may induce unexpected phenomena in both neutrino-flavor conversion and fluid dynamics. Addressing this issue would be important to gauge the sensitivity of FFCs to SNe and BNSMs. We also leave this exploration to future work.

ACKNOWLEDGMENTS

We are grateful to Lucas Johns and Masamichi Zazizen for useful comments and discussions. C.K. is supported by Grant-in-Aid for Early-Career Scientists (No.20K14457) and Grant-in-Aid for Scientific Research on Innovative Areas (No.22H04577). The numerical calculations were carried out on Yukawa-21 at YITP in Kyoto University and Cray XC50 at Center for Computational Astrophysics, National Astronomical Observatory of Japan.

-
- [1] S. Samuel, Neutrino oscillations in dense neutrino gases, *Phys. Rev. D* **48**, 1462 (1993).
 - [2] G. Sigl and G. Raffelt, General kinetic description of relativistic mixed neutrinos, *Nuclear Physics B* **406**, 423 (1993).
 - [3] G. Sigl, Neutrino mixing constraints and supernova nucleosynthesis, *Phys. Rev. D* **51**, 4035 (1995).
 - [4] R. F. Sawyer, Speed-up of neutrino transformations in a supernova environment, *Phys. Rev. D* **72**, 045003 (2005).
 - [5] T. Morinaga, Fast neutrino flavor instability and neutrino flavor lepton number crossings, arXiv e-prints, arXiv:2103.15267 (2021), arXiv:2103.15267 [hep-ph].
 - [6] B. Dasgupta, A. Mirizzi, and M. Sen, Fast neutrino flavor conversions near the supernova core with realistic flavor-dependent angular distributions, *J. Cosmology Astropart. Phys.* **2017**, 019 (2017), arXiv:1609.00528 [hep-ph].
 - [7] I. Tamborra, L. Hüdepohl, G. G. Raffelt, and H.-T. Janka, Flavor-dependent Neutrino Angular Distribu-

- tion in Core-collapse Supernovae, *ApJ* **839**, 132 (2017), [arXiv:1702.00060 \[astro-ph.HE\]](#).
- [8] M.-R. Wu, I. Tamborra, O. Just, and H.-T. Janka, Imprints of neutrino-pair flavor conversions on nucleosynthesis in ejecta from neutron-star merger remnants, *Phys. Rev. D* **96**, 123015 (2017).
- [9] B. Dasgupta, A. Mirizzi, and M. Sen, Simple method of diagnosing fast flavor conversions of supernova neutrinos, *Phys. Rev. D* **98**, 103001 (2018).
- [10] S. Abbar, H. Duan, K. Sumiyoshi, T. Takiwaki, and M. C. Volpe, On the occurrence of fast neutrino flavor conversions in multidimensional supernova models, *Phys. Rev. D* **100**, 043004 (2019), [arXiv:1812.06883 \[astro-ph.HE\]](#).
- [11] H. Nagakura, T. Morinaga, C. Kato, and S. Yamada, Fast-pairwise Collective Neutrino Oscillations Associated with Asymmetric Neutrino Emissions in Core-collapse Supernovae, *ApJ* **886**, 139 (2019), [arXiv:1910.04288 \[astro-ph.HE\]](#).
- [12] M. Delfan Azari, S. Yamada, T. Morinaga, W. Iwakami, H. Okawa, H. Nagakura, and K. Sumiyoshi, Linear analysis of fast-pairwise collective neutrino oscillations in core-collapse supernovae based on the results of Boltzmann simulations, *Phys. Rev. D* **99**, 103011 (2019), [arXiv:1902.07467 \[astro-ph.HE\]](#).
- [13] R. Glas, H.-T. Janka, F. Capozzi, M. Sen, B. Dasgupta, A. Mirizzi, and G. Sigl, Fast neutrino flavor instability in the neutron-star convection layer of three-dimensional supernova models, *Phys. Rev. D* **101**, 063001 (2020).
- [14] S. Abbar, H. Duan, K. Sumiyoshi, T. Takiwaki, and M. C. Volpe, Fast neutrino flavor conversion modes in multidimensional core-collapse supernova models: The role of the asymmetric neutrino distributions, *Phys. Rev. D* **101**, 043016 (2020).
- [15] S. Abbar, Searching for fast neutrino flavor conversion modes in core-collapse supernova simulations, *J. Cosmology Astropart. Phys.* **2020**, 027 (2020), [arXiv:2003.00969 \[astro-ph.HE\]](#).
- [16] T. Morinaga, H. Nagakura, C. Kato, and S. Yamada, Fast neutrino-flavor conversion in the preshock region of core-collapse supernovae, *Physical Review Research* **2**, 012046 (2020), [arXiv:1909.13131 \[astro-ph.HE\]](#).
- [17] M. Delfan Azari, S. Yamada, T. Morinaga, H. Nagakura, S. Furusawa, A. Harada, H. Okawa, W. Iwakami, and K. Sumiyoshi, Fast collective neutrino oscillations inside the neutrino sphere in core-collapse supernovae, *Phys. Rev. D* **101**, 023018 (2020), [arXiv:1910.06176 \[astro-ph.HE\]](#).
- [18] F. Capozzi, M. Chakraborty, S. Chakraborty, and M. Sen, Mu-tau neutrinos: Influencing fast flavor conversions in supernovae, *Phys. Rev. Lett.* **125**, 251801 (2020).
- [19] S. Abbar, F. Capozzi, R. Glas, H.-T. Janka, and I. Tamborra, On the characteristics of fast neutrino flavor instabilities in three-dimensional core-collapse supernova models, *Phys. Rev. D* **103**, 063033 (2021).
- [20] F. Capozzi, S. Abbar, R. Bollig, and H. T. Janka, Fast neutrino flavor conversions in one-dimensional core-collapse supernova models with and without muon creation, *Phys. Rev. D* **103**, 063013 (2021), [arXiv:2012.08525 \[astro-ph.HE\]](#).
- [21] H. Nagakura, A. Burrows, L. Johns, and G. M. Fuller, Where, when, and why: Occurrence of fast-pairwise collective neutrino oscillation in three-dimensional core-collapse supernova models, *Phys. Rev. D* **104**, 083025 (2021), [arXiv:2108.07281 \[astro-ph.HE\]](#).
- [22] A. Harada and H. Nagakura, Prospects of Fast Flavor Neutrino Conversion in Rotating Core-collapse Supernovae, *ApJ* **924**, 109 (2022), [arXiv:2110.08291 \[astro-ph.HE\]](#).
- [23] S. Richers, Evaluating Approximate Flavor Instability Metrics in Neutron Star Mergers, arXiv e-prints, [arXiv:2206.08444 \(2022\)](#), [arXiv:2206.08444 \[astro-ph.HE\]](#).
- [24] R. Akaho, A. Harada, H. Nagakura, W. Iwakami, H. Okawa, S. Furusawa, H. Matsufuru, K. Sumiyoshi, and S. Yamada, Protoneutron Star Convection Simulated with a New General Relativistic Boltzmann Neutrino Radiation-Hydrodynamics Code, arXiv e-prints, [arXiv:2206.01673 \(2022\)](#), [arXiv:2206.01673 \[astro-ph.HE\]](#).
- [25] M. George, M.-R. Wu, I. Tamborra, R. Ardevol-Pulpillo, and H.-T. Janka, Fast neutrino flavor conversion, ejecta properties, and nucleosynthesis in newly-formed hypermassive remnants of neutron-star mergers, *Phys. Rev. D* **102**, 103015 (2020).
- [26] X. Li and D. M. Siegel, Neutrino Fast Flavor Conversions in Neutron-Star Postmerger Accretion Disks, *Phys. Rev. Lett.* **126**, 251101 (2021), [arXiv:2103.02616 \[astro-ph.HE\]](#).
- [27] O. Just, S. Abbar, M.-R. Wu, I. Tamborra, H.-T. Janka, and F. Capozzi, Fast neutrino conversion in hydrodynamic simulations of neutrino-cooled accretion disks, *Phys. Rev. D* **105**, 083024 (2022), [arXiv:2203.16559 \[astro-ph.HE\]](#).
- [28] S. Abbar and M. C. Volpe, On fast neutrino flavor conversion modes in the nonlinear regime, *Physics Letters B* **790**, 545 (2019), [arXiv:1811.04215 \[astro-ph.HE\]](#).
- [29] J. D. Martin, C. Yi, and H. Duan, Dynamic fast flavor oscillation waves in dense neutrino gases, *Physics Letters B* **800**, 135088 (2020), [arXiv:1909.05225 \[hep-ph\]](#).
- [30] L. Johns, H. Nagakura, G. M. Fuller, and A. Burrows, Fast oscillations, collisionless relaxation, and spurious evolution of supernova neutrino flavor, *Phys. Rev. D* **102**, 103017 (2020), [arXiv:2009.09024 \[hep-ph\]](#).
- [31] S. Bhattacharyya and B. Dasgupta, Late-time behavior of fast neutrino oscillations, *Phys. Rev. D* **102**, 063018 (2020).
- [32] S. Bhattacharyya and B. Dasgupta, Fast Flavor Depolarization of Supernova Neutrinos, *Phys. Rev. Lett.* **126**, 061302 (2021), [arXiv:2009.03337 \[hep-ph\]](#).
- [33] S. Richers, D. E. Willcox, N. M. Ford, and A. Myers, Particle-in-cell simulation of the neutrino fast flavor instability, *Phys. Rev. D* **103**, 083013 (2021).
- [34] S. Richers, D. Willcox, and N. Ford, Neutrino fast flavor instability in three dimensions, *Phys. Rev. D* **104**, 103023 (2021), [arXiv:2109.08631 \[astro-ph.HE\]](#).
- [35] M.-R. Wu, M. George, C.-Y. Lin, and Z. Xiong, Collective fast neutrino flavor conversions in a 1D box: Initial conditions and long-term evolution, *Phys. Rev. D* **104**, 103003 (2021),

- arXiv:2108.09886 [hep-ph].
- [36] S. A. Richers, G. C. McLaughlin, J. P. Kneller, and A. Vlasenko, Neutrino quantum kinetics in compact objects, *Phys. Rev. D* **99**, 123014 (2019), arXiv:1903.00022 [astro-ph.HE].
- [37] S. Shalgar and I. Tamborra, Dispelling a myth on dense neutrino media: fast pairwise conversions depend on energy, *J. Cosmology Astropart. Phys.* **2021**, 014 (2021), arXiv:2007.07926 [astro-ph.HE].
- [38] J. D. Martin, J. Carlson, V. Cirigliano, and H. Duan, Fast flavor oscillations in dense neutrino media with collisions, *Phys. Rev. D* **103**, 063001 (2021), arXiv:2101.01278 [hep-ph].
- [39] M. Zaizen and T. Morinaga, Nonlinear evolution of fast neutrino flavor conversion in the preshock region of core-collapse supernovae, arXiv e-prints, arXiv:2104.10532 (2021), arXiv:2104.10532 [hep-ph].
- [40] S. Bhattacharyya and B. Dasgupta, Elaborating the Ultimate Fate of Fast Collective Neutrino Flavor Oscillations, arXiv e-prints, arXiv:2205.05129 (2022), arXiv:2205.05129 [hep-ph].
- [41] S. Abbar and F. Capozzi, Suppression of fast neutrino flavor conversions occurring at large distances in core-collapse supernovae, *J. Cosmology Astropart. Phys.* **2022**, 051 (2022), arXiv:2111.14880 [astro-ph.HE].
- [42] H. Nagakura and M. Zaizen, Time-dependent, quasi-steady, and global features of fast neutrino-flavor conversion, arXiv e-prints, arXiv:2206.04097 (2022), arXiv:2206.04097 [astro-ph.HE].
- [43] S. Shalgar and I. Tamborra, Supernova Neutrino Decoupling Is Altered by Flavor Conversion, arXiv e-prints, arXiv:2206.00676 (2022), arXiv:2206.00676 [astro-ph.HE].
- [44] S. Shalgar and I. Tamborra, Neutrino Flavor Conversion, Advection, and Collisions: The Full Solution, arXiv e-prints, arXiv:2207.04058 (2022), arXiv:2207.04058 [astro-ph.HE].
- [45] S. Shalgar and I. Tamborra, Change of direction in pairwise neutrino conversion physics: The effect of collisions, *Phys. Rev. D* **103**, 063002 (2021), arXiv:2011.00004 [astro-ph.HE].
- [46] C. Kato, H. Nagakura, and T. Morinaga, Neutrino Transport with the Monte Carlo Method. II. Quantum Kinetic Equations, *ApJS* **257**, 55 (2021), arXiv:2108.06356 [astro-ph.HE].
- [47] H. Sasaki and T. Takiwaki, Dynamics of fast neutrino flavor conversions with scattering effects: a detailed analysis, arXiv e-prints, arXiv:2109.14011 (2021), arXiv:2109.14011 [hep-ph].
- [48] G. Sigl, Simulations of fast neutrino flavor conversions with interactions in inhomogeneous media, *Phys. Rev. D* **105**, 043005 (2022), arXiv:2109.00091 [hep-ph].
- [49] R. S. L. Hansen, S. Shalgar, and I. Tamborra, Enhancement or damping of fast neutrino flavor conversions due to collisions, *Phys. Rev. D* **105**, 123003 (2022), arXiv:2204.11873 [astro-ph.HE].
- [50] L. Johns and H. Nagakura, Self-consistency in models of neutrino scattering and fast flavor conversion, arXiv e-prints, arXiv:2206.09225 (2022), arXiv:2206.09225 [hep-ph].
- [51] L. Johns, Collisional flavor instabilities of supernova neutrinos, arXiv e-prints, arXiv:2104.11369 (2021), arXiv:2104.11369 [hep-ph].
- [52] C. Volpe, Neutrino quantum kinetic equations, *International Journal of Modern Physics E* **24**, 1541009 (2015), arXiv:1506.06222 [astro-ph.SR].
- [53] C. Kato, H. Nagakura, Y. Hori, and S. Yamada, Neutrino Transport with Monte Carlo Method. I. Toward Fully Consistent Implementation of Nucleon Recoils in Core-collapse Supernova Simulations, *ApJ* **897**, 43 (2020), arXiv:2001.11148 [astro-ph.HE].
- [54] I. Padilla-Gay, I. Tamborra, and G. G. Raffelt, Neutrino Flavor Pendulum Reloaded: The Case of Fast Pairwise Conversion, *Phys. Rev. Lett.* **128**, 121102 (2022), arXiv:2109.14627 [astro-ph.HE].
- [55] L. Johns, H. Nagakura, G. M. Fuller, and A. Burrows, Neutrino oscillations in supernovae: Angular moments and fast instabilities, *Phys. Rev. D* **101**, 043009 (2020), arXiv:1910.05682 [hep-ph].